Metabolic–epigenetic rewiring driven by MCT4-mediated lactate export contributes to resistance to PD-1 blockade in NSCLC

Huiyu Wang [a, b, d], Xiaomin Niu [c], Hua Xiao [d], Shen S. Hu [a, b, *]

[a] Zhejiang Key Laboratory of Multiomics and Molecular Enzymology, Yangtze Delta Region Institute of Tsinghua University, Zhejiang, 314006, China.

[b] Department of Biotechnology and Biomedicine, Yangtze Delta Region Institute of Tsinghua University, Zhejiang, 314006, China.

[c] Department of Shanghai Lung Cancer Center, Shanghai Chest Hospital, Shanghai Jiao Tong University School of Medicine, Shanghai, 200030, China

[d] State Key Laboratory of Microbial Metabolism, Joint International Research Laboratory of Metabolic & Developmental Sciences, School of Life Sciences and Biotechnology, Shanghai Jiao Tong University, Shanghai, 200240, China.

* Corresponding Author:

Professor Shen S. Hu, Email: hushen@tsinghua-zj.edu.cn

Abstract

Resistance to PD-1 blockade remains a major obstacle in non-small cell lung cancer (NSCLC) treatment. To understand the molecular mechanisms underlying immunotherapy resistance, we performed integrative transcriptomic and proteomic analyses of clinical tumor samples from immunotherapy responders and nonresponders. Tumors from nonresponders exhibited increased glycolytic activity and expression of the lactate transporter MCT4, which correlated with reduced $CD8^+$ T-cell infiltration and unfavorable clinical outcomes. In highly glycolytic NSCLC cell models, *MCT4* deficiency not only restored $CD8^+$ T-cell proliferation and effector function but also induced tumor-intrinsic mitochondrial stress, characterized by increased reactive oxygen species levels, reduced ATP production, and loss of mitochondrial membrane potential, ultimately leading to G2/M cell cycle arrest. Mechanistically, *MCT4* deficiency activated the EHMT2/H3K9me3 axis, resulting in the transcriptional repression of genes that govern cell cycle progression. Importantly, pharmacological inhibition of MCT4 produced comparable effects. Collectively, these findings indicate that the lactate transporter MCT4 suppresses antitumor immunity and that targeting MCT4 represents a promising strategy to overcome immunotherapy resistance in patients with highly glycolytic NSCLC.

Introduction

Lung cancer is the leading cause of cancer death worldwide, with 2.5 million new cases each year, accounting for 12.4% of the total new cancer cases [1]. Non-small cell lung cancer (NSCLC) accounts for approximately 85% of all lung cancer cases and encompasses a heterogeneous group of histological subtypes, including adenocarcinoma and squamous cell carcinoma [2]. PD-(L)1 immune checkpoint blockade has revolutionized the treatment of NSCLC, generating profound and durable clinical responses and rapidly becoming a cornerstone of therapy for patients with advanced-stage disease [3, 4]. However, a subset of patients, estimated to be 5–20%, exhibit primary resistance to PD-1 blockade, defined as a lack of clinical response to immune checkpoint inhibitors (ICIs) from treatment initiation, which has been associated with preexisting genetic or epigenetic alterations within tumor cells and/or the tumor microenvironment [5-7].

Increasing evidence suggests that, beyond immune cell dysfunction, metabolic reprogramming within tumor cells plays a pivotal role in shaping the immunosuppressive tumor microenvironment and limiting the efficacy of immune checkpoint inhibition [8]. In particular, increased glycolysis is a hallmark of malignant cells and results in excessive lactate production, particularly under hypoxic conditions [9]. Excessive lactate accumulation perturbs tumor microenvironmental homeostasis and directly compromises immune effector cell function [10]. Emerging evidence supports a central role for dysregulated lactate metabolism in immune evasion, mediated by impaired $CD8^+$ T-cell proliferation and cytotoxicity and increased recruitment of regulatory T cells and myeloid-derived suppressor cells [11, 12]. Monocarboxylate transporter 4 (MCT4, encoded by SLC16A3) is thought to be the primary mediator of lactic acid transport across the plasma membrane, which is fundamental for maintaining glycolytic flux [13]. MCT4 is

overexpressed in several types of cancers, including NSCLC, and serves as an independent negative prognostic factor [14]. However, the effects of increased lactate production and MCT4-mediated lactate secretion on immunotherapy resistance are unknown.

Beyond its metabolic functions, lactate has emerged as a critical regulator of epigenetic states in cancer cells [15]. Histone lactylation, an epigenetic modification induced by glycolytic activity, has been increasingly linked to the activation of gene expression [16]. Zang *et al*. demonstrated that H3K18 lactylation promotes immunosuppression in NSCLC cells by inducing POM121 expression, thereby increasing MYC activity and PD-L1 expression; notably, this immunosuppressive program can be reversed through metabolic reprogramming and immunotherapy [8]. Similarly, Wang *et al*. reported that lactate accumulation drives H3K9 lactylation and subsequent IL-11 activation, leading to $CD8^+$ T-cell exhaustion via the JAK2–STAT3 signaling pathway [9]. In addition to histone lactylation, emerging evidence suggests that lactate can modulate other histone modifications to reshape immune responses. Shi *et al.* reported that upon lipopolysaccharide (LPS) stimulation, lactic acid serves as a major carbon source for tricarboxylic acid (TCA) cycle metabolism, thereby promoting epigenetic reprogramming through histone H3K27 acetylation. Collectively, these findings establish lactate as a central metabolic–epigenetic regulator that orchestrates diverse histone modifications to drive immunosuppressive programs; however, whether lactate metabolism also alters repressive chromatin mechanisms to regulate tumor cell-intrinsic fate under immunotherapeutic pressure remains unclear.

In this study, we integrate clinical multiomics analyses, genetic and pharmacological perturbations, and epigenomic profiling to investigate the role of MCT4 in regulating tumor cell-intrinsic responses to anti-PD-1 therapy. We demonstrate that MCT4-dependent lactate secretion drives EHMT2-mediated H3K9me3 reprogramming, leading to coordinated repression of cell cycle licensing and mitochondrial metabolic programs, thereby promoting G2/M arrest without inducing apoptosis. Importantly, pharmacological inhibition of MCT4 restores tumor sensitivity to anti-PD-1 therapy by alleviating metabolic and epigenetic constraints on antitumor immunity. Our findings reveal a previously unrecognized MCT4–EHMT2/H3K9me axis that links tumor metabolism, chromatin regulation, and immunotherapy resistance, providing a rational basis for combining metabolic–epigenetic strategies to increase immune checkpoint blockade efficacy in NSCLC patients.

Method details

Clinical specimens

Clinical samples from NSCLC patients who received PD-1/PD-L1 immunotherapy at Shanghai Chest Hospital, Shanghai Jiao Tong University School of Medicine, were collected between 2018 to 2024. On the basis of the clinical efficacy of immune checkpoint blockade, treatment responses were evaluated according to the RECIST criteria [17], using progression-free survival (PFS) and overall survival (OS) as endpoints. Patients were divided into a responder group (PFS > 6 months) and a resistant group

(PFS < 6 months) [18]. Integrated transcriptomic and proteomic analyses, combined with GSVA, KEGG pathway enrichment, protein–protein interaction network analysis, and metabolic pathway profiling, were performed to systematically delineate key signaling pathways and molecular characteristics associated with immunotherapy resistance, providing a foundation for subsequent mechanistic studies. This study was approved by the Ethics Committee of Shanghai Ninth People's Hospital affiliated with Shanghai Jiao Tong University School of Medicine. Written informed consent was obtained from all patients.

RNA isolation, library preparation and sequencing

Total RNA was extracted from the tissues by using TRIzol® reagent according to the manufacturer's instructions. The quality of the RNA was assessed using a 5300 Bioanalyzer (Agilent). Small RNA libraries were produced with the QIAseq miRNA Library Kit (Qiagen) according to the manufacturer's guidelines. Furthermore, mRNA, lncRNA, and circRNA libraries were prepared using the Illumina Stranded Total RNA Prep with Ribo-Zero Plus. Subsequent sequencing was conducted by Shanghai Majorbio Bio-pharm Biotechnology Co., Ltd. (Shanghai, China) on an Illumina NovaSeq 6000 platform. Data analysis was performed using the Majorbio Cloud (www.majorbio.com).

Protein digestion and proteomics analysis

Tissue samples were suspended in protein lysis buffer (8 M urea, 1% SDS), homogenized, reduced, and alkylated [19]. After trypsin digestion, the peptides were mixed and analyzed by a Vanquish Neo system coupled with an Orbitrap Astral mass spectrometer (Thermo, USA) using data-dependent acquisition for library construction. Data-independent acquisition was performed for each sample using an Orbitrap Astral mass spectrometer operated in DIA mode. MS data were collected over an m/z range of 100–1700. The aw DIA data were subjected to a search using Spectronaut software (version 19). Three peptides per protein and 3 daughter ions per peptide were selected for quantitative analysis. The parameters were as follows: protein FDR≤0.01, peptide FDR≤0.01, peptide confidence ≥99%, and XIC width ≤75 ppm. Peptides that were shared among groups and those that were modified were excluded, and the peak areas were calculated and summed for quantification. Only the proteins that had at least one unique peptide were used for protein identification. Data analysis was performed using the Majorbio Cloud (www.majorbio.com).

Cell lines and cell culture

LLC cells were cultured in DMEM (Gibco, MA, USA) supplemented with 10% FBS and 1% penicillin/streptomycin (Gibco) before use. CTLL2 and $CD8^+$ T cells were cultured in RPMI-1640 medium (Gibco) supplemented with 10% FBS, 1% penicillin/streptomycin (Gibco), 100 U of IL-20 and 0.05 mM β-mercaptoethanol. The cell cultures were maintained at 37°C in a 5% CO_2 environment.

Construction of the MCT4-Knockout Cell Line

The guide-RNA (gRNA, 5'-GACTGTAATGTTGCTTTCTCG-3') was designed by an online CRISPR design tool (https://zlab.bio/guide-design-resources). Two partially complementary oligonucleotides (5'-CACCGTGGTGGACGAGGGTCCCAC-3' and 5'-AAACGTGGGACCCTCGTCCACCAC-3') were annealed, cloned and inserted into the PX459 plasmid (Addgene, #62988), which had been predigested with the BbsI restriction enzyme. This construct was denoted the *MCT4*-KO plasmid, which could guide hSpCas9 to the genomic target site in the *MCT4* gene.

A total of 2.5 μg of *MCT4*-KO and PX459 plasmids (control) were transfected into 1×10^6 LLC cells with Lipofectamine 3000 reagent (Thermo Fisher), and the medium was exchanged for fresh complete medium 12 h later. After 48 h of culture, the cells were incubated in fresh medium supplemented with 2 μg/mL puromycin. Seven days later, cells that were resistant to puromycin were selected. Western blot analysis was used to determine knockout efficiency. Single cells were subsequently obtained by the limited dilution method, and the knockout efficiency was verified by DNA sequencing (primer: 5'-AGTGGAGATGGCATTGTCCG-3'). On the basis of the Western blotting and DNA sequencing results, two *MCT4*-knockout cell lines were selected for experiments.

RNA extraction and quantitative real-time PCR (qRT–PCR) analysis

Total RNA was extracted using TRIzol reagent (Invitrogen) following the manufacturer's protocol. cDNA was synthesized from 1 μg of total RNA using HiScript II Q RT SuperMix (Vazyme, R233-01). The primers used were designed with the PrimerBank database (https://pga.mgh.harvard.edu/primerbank/), and the sequences are listed in Table S1. Amplicon sizes ranged from 90 to 150 bp. qPCRs were performed in a 20 μL reaction volume containing 10 μL of SYBR Green Master Mix (YEASEN, #11185), 0.5 μL each of forward and reverse primers (10 μM), 2 μL of cDNA template, and 7 μL of nuclease-free water. Reactions were performed with six technical replicates for each sample on a qTOWER3 touch real-time PCR thermal cycler (Analytik Jena AG, Germany). β-Actin served as the internal control, and relative mRNA expression levels were calculated using the $2^{-\Delta\Delta Ct}$ method. No-template controls confirmed the absence of contamination and genomic DNA.

Mouse $CD8^+$ T cell isolation

A mouse $CD8a^+$ T-cell isolation kit (130-104-075; Miltenyi) was used to isolate mouse $CD8^+$ T cells from the spleens of healthy controls. In brief, single cells from the spleen were incubated with a biotinylated antibody cocktail and anti-biotin microbeads at 4°C and then isolated with a MidiMACS Separator to collect CD8+ T cells. Next, the cells were stimulated with 2 μg/mL anti-mouse CD3 and anti-mouse CD28 antibodies (130-093-627; Miltenyi) for 3 days and with recombinant mouse IL-2 (212-12; PeproTech) and 0.05 mM mercaptoethanol for another 4 days. Then, LLC cells, *MCT4*-KO LLC cells or 10 mM sodium lactate were added to the activated $CD8^+$ T cells for coculture at a ratio of 1:3 under anti-CD3/CD28 stimulation.

Mouse tumor models

C57BL/6J mice (4–5 weeks of age, female, Shanghai) were housed in a specific pathogen-free facility; the experimental procedures were approved by the Institutional Animal Care and Use Committee at Shanghai Jiaotong University. For *in vivo* experiments, control or *MCT4*-KO LLC cells (1×10^6/mouse) were implanted subcutaneously into C57BL/6J mice. For immunotherapy, tumor-bearing mice were administered 100 μg of anti-PD-1 antibody or the control treatment every third day when the tumor reached 80 mm^3. For the combination therapy regimen, C57BL/6J mice were implanted subcutaneously with 1×10^6 LLC cells and intraperitoneally administered 100 μg of anti-PD-1 antibody every third day and 0.2 mg/kg MSC-4381 (an MCT4 inhibitor) daily when the tumors reached 80 mm^3. Tumor volumes were measured using the formula $V=ab^2/2$ (a, major axis; b, minor axis).

Flow cytometry

For surface marker analysis, samples were stained with buffer containing fluorescently labeled antibodies against CD45, CD3, CD8, and PD-L1 (Supplementary Table S2). For intracellular staining, the samples were incubated with Leukocyte Activation Cocktail (550583; BD Pharmingen) at 37°C for 4 to 6 hours, fixed and permeabilized with a Transcription Factor Buffer Set (562574; BD Pharmingen), followed by staining with antibodies against Ki67, GzMB, and IFNγ. Data were acquired using a BD Fortessa flow cytometer (BD Biosciences).

For the tumor-infiltrating lymphocyte staining assays, the cell samples were incubated with specific antibodies against surface markers and intracellular markers. For mouse tumor samples, the antibodies used included anti-mouse CD45-Percp-Cy5.5 (103132), anti-mouse CD4-Percp-Cy5.5 9 (BD, 550954), anti-mouse CD25-BV786 (BD, 564368), anti-mouse FOXP3-PE (BD, 560408), anti-mouse CD45 APC-CY7 (BD, 557659) anti-mouse CD3-FITC (BD, 553061), anti-mouse F4/80-BV421 (BD, 565411), anti-mouse CD11b-BV605 (BD, 563015), anti-mouse CD49b-APC (BD, 560628), anti-mouse CD19-BV650 (BD, 563235), and anti-mouse CD8-AF700 (BD, 566985), and intracellular antibodies, including anti-mouse IFNγ (BD, 570731), anti-mouse GzMB (Thermo, 12-8898-82), and anti-mouse KI-67 (BD Pharmingen, 561126). The data were analyzed using FlowJo 10.8.1.

CUT&Tag

In accordance with the manufacturer's instructions for the CUT&Tag kit (cat# 53170; Active Motif, CA, USA), a hyperactive *in situ* ChIP Library Prep Kit for Illumina (pG-Tn5) (TD901; Vazyme Biotech, China) was used for the CUT&Tag assay. Briefly, after treatment, LLC and *MCT4*-KO LLC cells were collected and bound to concanavalin A beads. The cells were then incubated with an anti-H3K9me3 primary antibody (13969T, CST), followed by incubation with secondary antibodies. Then, pA-Tn5 transposase was added to the processed samples. After activation of Tn5 transposase-mediated transposition, the DNA was extracted and amplified to construct a DNA library. VAHTS

DNA Clean beads (N411; Vazyme Biotech) were used for DNA purification. The library was quantified using the VAHTS Library Quantification Kit for Illumina (Vazyme Biotech), and library sequencing was conducted using the Illumina NovaSeq 150 PE platform. The data were analyzed by Sangon Biotech (Shanghai, China).

CHIP–qPCR

For H3K9me3 ChIP–qPCR, a BeyoChIP™ ChIP Assay Kit (cat# P2078; Beyotime, China) was used. Briefly, after treatment, the cells were individually cross-linked with 1% formaldehyde for 10 min at 37°C and quenched by the addition of glycine at a final concentration of 0.125 M. The cross-linked cells were rinsed twice with PBS, lysed in ChIP lysis buffer, and then sonicated into 150–300 bp fragments (150 W, 55 s on and 10 s off). The supernatant was diluted tenfold and then incubated with H3K9me3 antibody overnight at 4°C, after which protein A/G magnetic Dynabeads were added to capture the immunoprecipitates. The beads were subsequently washed with low-salt buffer, high-salt buffer, LiCl buffer, and TE buffer. The DNA was eluted from the washed beads with elution buffer at 65 °C after vortexing for 30 min. Supernatants were incubated at 65 °C for 4–6 h to reverse the crosslinking and release the immunoprecipitated DNA. After incubation with RNase A and proteinase K, DNA was purified with a DNA Purification Kit (cat# P2080S; Beyotime, China). The primers used for ChIP–qPCR are listed in Supplementary Data 2. The antibodies used for ChIP were as follows: anti-H39me3 (CST, # 13969) and rabbit anti-IgG (Beyotime, A7016); 5 μg of the antibodies against H3K9me3 and control IgG were applied to the lysates from 1×10^7 cells.

Measurement of lactate levels

To measure the lactate content in LLC and *MCT4*-KO LLC cells after different treatments *in vitro*, cells were seeded into 6-well plates, and then, equal amounts of cells were washed with PBS three times, harvested with a cell scraper in extraction buffer, dissociated by sonication, and centrifuged for 10 minutes at 12,000 × *g*, after which the supernatant was collected for measurement of the intracellular lactate concentration using a lactate quantification kit (A01921, NJJCBIO). To measure intratumoral lactate levels, tumor tissues were weighed and homogenized with a tissue homogenizer in PBS and centrifuged at 12,000 × g for 10 minutes to collect the supernatant. The lactate content in the supernatant was subsequently determined with a lactate quantification kit (A01921; NJJCBIO). The final intratumoral lactate levels were normalized to the protein concentration in the tumor. The lactate concentration was then determined from measurements made using a multifunctional microplate reader (Infinite 200 Pro, Tecan) at a reference wavelength of 530 nm.

Phosphoproteomic analysis

Total proteins from LLC and LLC *MCT4*-KO cells were digested with trypsin (Promega, V5111) overnight at 37°C using the filter-aided sample preparation (FASP) approach as previously described [20]. Phosphorylated peptides were enriched by titanium (IV)

ion-immobilized metal ion affinity chromatography (Ti^{4+}-IMAC) according to the manufacturer's protocol [21] at an IMAC material (J&K Scientific, 2749380) to Ti^{4+} (Sinopharm chemical, 10022728) ratio of 1:100 (w/w). After centrifugation at 15,000 × g for 5 min, 300 μg of the digested peptides was mixed with the prepared Ti^{4+}-IMAC material at a ratio of 1:25 (w/w) and vortexed for 30 min. Then, the supernatant was removed after centrifugation at 15,000 × g for 5 min. The pellet was subsequently washed twice with Washing Buffer 1 (50% ACN with 6% TFA and 200 mM NaCl) followed by Washing Buffer 2 (30% ACN with 0.1% TFA). The phosphorylated peptides captured on the Ti^{4+}-IMAC material were eluted with 10% $NH_3 \cdot H_2O$ using ultrasonication and vortexing. Eluted phosphorylated peptides were dried with a rotary evaporator. Afterward, the total and phosphorylated peptides were desalted on ZipTip C18 column (Millipore, Billerica, MA, USA) and analyzed using an Easy-nanoLC1000 instrument (250 mm × 50 μm column packed with 3 μm C18-AQ particles) coupled with an Orbitrap Q Exactive Plus mass spectrometer (Thermo Fisher Scientific).

Animal study

For the subcutaneous tumor model, 1×10^5 SCCVII cells were injected into the flanks of mice, with or without the indicated treatments. The length (L) and width (W) of the tumors were measured every two or three days beginning on the 15th day after injection, and the volume was calculated as $L \times W^2$. For drug treatment, L-lactate (15 mM, i.t., once a day) (L1750, Sigma–Aldrich, MO, USA), anti-CD8 antibody (150 μg, i.p., once every three days) (C375, Leinco, MO, USA) and anti-PD1 antibody (150 μg, i.p., once every three days) (BE0146, BioXCell, NH, USA) were injected into the mice. Cholesterol-conjugated siIL11 (RiboBio) was injected subcutaneously (10 nmol per tumor nodule, i.t.) once every two days. When the tumor volume reached 2,000 mm^3, which is equivalent to a humane treatment endpoint, the mice were euthanized. Treatment efficacy was estimated by analyzing the survival curves.

Immunoblotting

The immunoblotting procedure was performed in accordance with the protocol described in our previous study [22]. The primary antibodies against L-lactyl lysine (pan-Kla; PTM-1401RM) was purchased from PTM Bio; those against EHMT2 (#3306T), H3K9me1 (#14186T), H3K9me2 (#4658T), and H3K9me3 (#139695) were purchased from Cell Signaling Technology; that against MCT4 (#S0B0893) and histone H3 (#S0B0756) were purchased from Starter; that against β-actin (#30101ES60) was purchased from Yeasen; and those against LDHA (#21799-1-AP) and GAPDH (#60004-1) were purchased from Proteintech.

Multiplex immunofluorescence assays

Formalin-fixed, paraffin-embedded specimens were subjected to sequential immunostaining. The tissues were incubated with primary antibodies overnight and then with secondary antibodies for 1 h at 20–26°C, followed by microwave treatment and re-staining with the primary antibodies. The following antibodies were used: anti-EHMT2

rabbit antibody (ab185050, Abcam), anti-SLC16A3/MCT4 rabbit antibody (ab308528, Abcam), and anti-L-lactyl lysine rabbit polyclonal antibody (S0B0719, STARTER); the nuclear dye DAPI (D21490, Thermo Fisher Scientific) was also applied.

Measurement of ROS levels

Intracellular ROS levels were measured using a DCFH-DA fluorescent probe (10 μM; Beyotime, S0033). LLC WT and *MCT4-KO* cells were incubated with 10 μM DCFH-DA at 37 °C for 30 minutes in the dark. Afterward, the cells were collected, washed, and resuspended in PBS. For inhibitor treatment, cells were pretreated with the MCT4 inhibitor AZD0095 for 48 h prior to subsequent experiments. ROS levels were evaluated by flow cytometry (CytoFLEX, Beckman Coulter Co., Ltd.). A total of 10,000 events were collected per sample. The data were analyzed using FlowJo software (version 10.8.1).

Measurement of intracellular ATP levels

The total cellular ATP level was determined on the basis of luciferase (Beyotime, S0027) intensity following the manufacturer's instructions. Luciferase can catalyze the reaction between ATP and luciferin and generate light intensity that is proportional to the ATP concentration [23]. Briefly, after treatment, the cells were lysed with lysis buffer and incubated at room temperature for 5 minutes to release cellular ATP. The supernatant was then mixed with the luciferase detection reagent, and luminescence was immediately measured using a multimode microplate reader (Spark, Tecan).

Measurement of mtDNA copy number

mtDNA copy number was determined by quantitative real-time PCR (qPCR) following the method described by Jackson *et al*. with minor modifications [24]. Primer pairs specific for mitochondrial-encoded genes (mitochondrial NADH dehydrogenase 1, mt-ND1; and Cytochrome c oxidase polypeptide I, CO1) and nuclear-encoded genes (β2-microglobulin and β2-MG) were used. qPCR was performed as previously described. Nuclear DNA (nDNA) served as an internal control, and the relative mtDNA copy number was calculated using the $2^{-\Delta Ct}$ method (ΔCt = Ct_mtDNA – Ct_nDNA) [25]. The primer sequences are listed in Supplementary Table 1.

Results

2.1 Distinct transcriptomic and proteomic landscapes associated with resistance to immunotherapy in NSCLC

Among 127 patients with NSCLC treated with PD-1 blockade at Shanghai Chest Hospital between April 2018 and August 2014, 70 (54%) failed to derive clinical benefit (Supplementary Table 1). We performed a statistical analysis of the clinical information and related indicators of the patients prior to treatment that did and did not exhibit a clinical response to PD-1 blockade and found that several baseline clinical and pathological features differed between responders and nonresponders (Figure 1A). Compared with nonresponders, responders exhibited higher intratumoral PD-L1 protein

expression (54% vs. 36%, Fisher's $p < 0.01$) and a lower overall frequency of gene mutations (21% vs. 34%, Fisher's $p < 0.01$). The organ-specific pattern of progression also differed, with liver metastases common among nonresponders but relatively uncommon among responders (9% vs. 2%, odds ratio 4.5, Fisher's $p < 0.001$; Figure 1B). Progression-free survival (PFS) was significantly longer for patients who responded to PD-1 blockade than for those who did not respond (median 349 days vs. 88 days, Figure 1C and Figure S1A, S1B).

To elucidate the molecular mechanism underlying the therapeutic response, multiomic profiling was performed on tumor samples from 30 patients (12 responders and 18 nonresponders) (Figure 1D). A total of 19,153 transcripts and 9,157 proteins were identified (Figure 1E). Among them, 46 genes exhibited concordant differential abundance at both the mRNA and protein levels between responders and nonresponders (Figure 1E, 1F). Notably, principal component analysis (PCA) demonstrated that compared with the transcriptomic profiles, the proteomic data exhibited a clearer separation between responders and nonresponders (Figure 1G, 1H and Figure S1C-S1E), indicating that posttranscriptional regulation may play a critical role in shaping the molecular heterogeneity underlying the response to PD-1 blockade. We next analyzed the tumor immune microenvironment using CIBERSORT-based deconvolution of the bulk transcriptomic data. Distinct immune cell infiltration patterns were observed between the groups, as nonresponders displayed reduced numbers of activated NK cells and $CD8^+$ T cells. (Figure 1J, Figure S1F). The overall immune score, a reflection of immune cell abundance, was significantly greater in responders than in nonresponders (Figure 1K). On the basis of previously reported data [6, 7], integrated analysis of ICB chemotherapy in both responders and nonresponders and single-cell RNA sequencing and spatial transcriptomic analyses revealed that nonresponders exhibited a markedly lower proportion of $CD8^+$ T cells, suggesting that insufficient cytotoxic T-cell infiltration may underlie the reduced efficacy of ICB therapy.

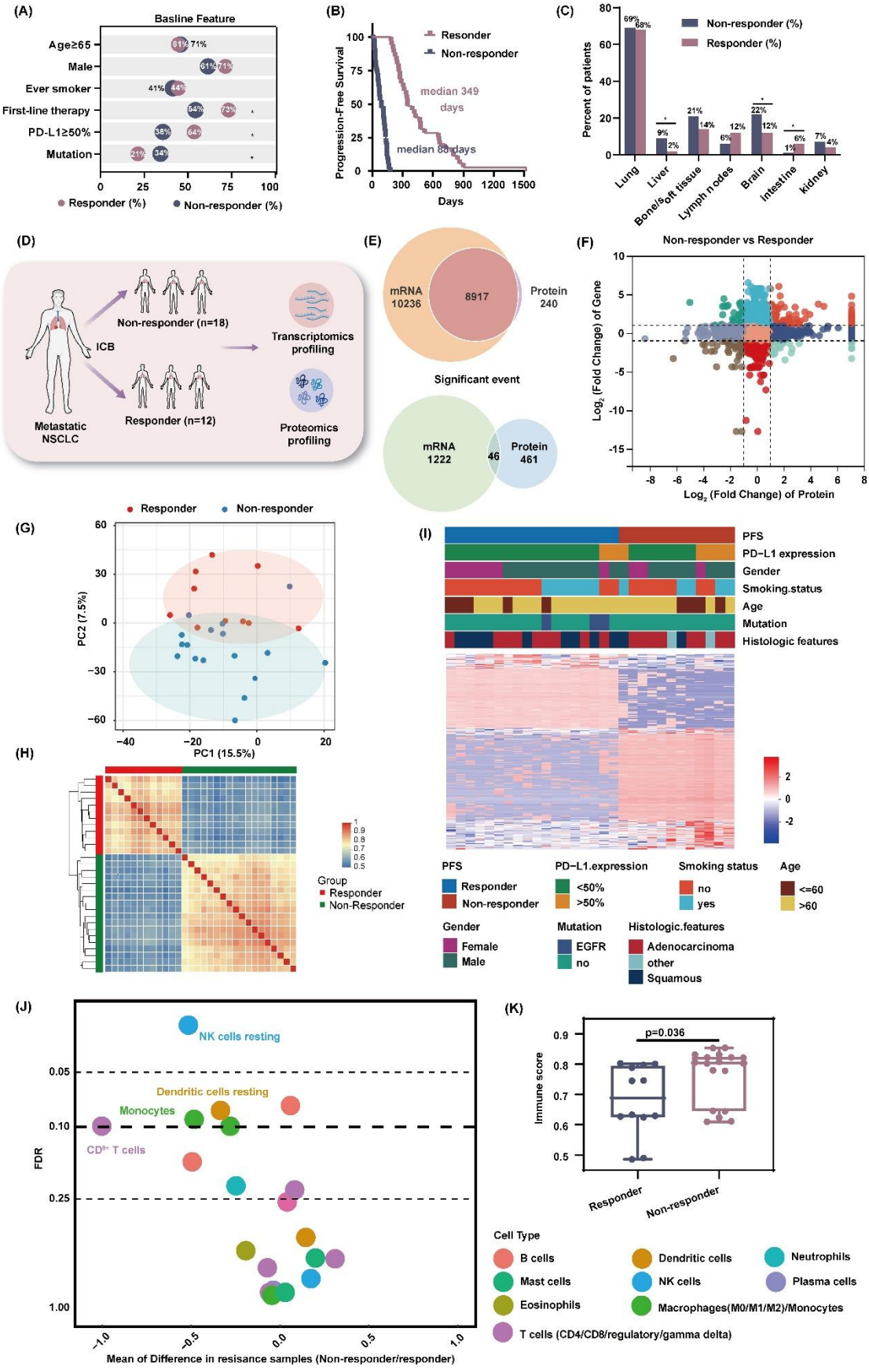

Figure 1. Clinical and multiomics features of lung cancer patients who did and did not respond to immunotherapy. (A) Rates of baseline clinical features among responders (n = 57) and nonresponders

(n = 70). (B) Progression-free survival of responders and nonresponders. (C) Common sites of metastasis in responders and nonresponders. (D) Workflow of the research design. We integrated transcriptomics and proteomics data from both responders (n=12) and nonresponders (n=18). (E) Venn diagrams depicting the identified and differentially expressed mRNAs and proteins. (F) Scatterplot comparing the changes in abundance between mRNAs and their corresponding proteins. (G) Principal component analysis of the proteomic data of responder and nonresponder samples. (H) Pearson's correlation of the responder and nonresponder samples for the proteomics data. (I) Heatmap of differentially expressed factors and corresponding clinical information. (J) Comparison of different immune cell estimates (CIBERSORT) between responders and nonresponders. Each point represents an immune cell type, and the associated color reference is indicated in the panel. (K) Immune scores of responders and nonresponders.

2.2 Activation of glycolysis and hypoxia pathways are potential mechanisms of the nonresponse to ICB

We summarized gene expression values into pathway-level scores using single-sample gene set enrichment analysis (ssGSEA)[26] on hallmark [27] gene sets and KEGG gene sets [28]. Differential expression analysis of hallmark gene sets revealed significant upregulation of genes associated with IL6-JAK-STAT3, glycolysis, oxidative phosphorylation, TNF-α signaling via NF-κB, fatty acid metabolism, and hypoxia in the nonresponder group (Figure 2A and Figure S2A). Glycolysis is increasingly being recognized as a pivotal metabolic program that drives tumor progression and immune evasion [29]. Recent studies have linked high glycolytic activity with resistance to immune checkpoint blockade therapy, suggesting that tumor metabolic reprogramming may underlie primary or acquired immunotherapy resistance [30, 31]. To further characterize glycolytic dysregulation in our cohort, we applied CIBERSORT to calculate Spearman correlation coefficients between the differentially expressed glycolysis-related genes (including *HK2*, *LDHA*, and *SLC16A3*) and immune cell subsets in the tumor microenvironment (Figure 2B). Notably, the expression levels of SLC16A3 (MCT4), LDHA, and HK2 were negatively correlated with the $CD8^+$ T-cell subsets. We further evaluated the prognostic relevance of these glycolysis-related genes using TCGA datasets. Survival analysis of both lung squamous cell carcinoma (LUSC) and lung adenocarcinoma (LUAD) cohorts revealed that high expression of SLC16A3 (MCT4), LDHA, and SLC16A1 (MCT1) was significantly associated with reduced overall survival ($P < 0.05$; Figure S2x). Monocarboxylate transporter 4 (SLC16A3, MCT4) is a proton-linked lactate exporter that facilitates the efflux of lactate and protons from highly glycolytic tumor cells[32]. Elevated SLC16A3 expression is associated with hypoxia-driven metabolic reprogramming, immune suppression, and poor prognosis in multiple cancers, including lung cancer [13, 33].

We next measured the intracellular lactate concentration in tumor samples and found that the nonresponder group had significantly higher lactate levels than the responder group did ($P < 0.05$; Figure 2C). Immunoblot analysis revealed markedly elevated pan-lactylation (pan-Kla) levels and MCT4 protein expression in nonresponders compared

with responders, confirming the increased glycolytic flux and lactate accumulation at the protein level (Figure 2D). Consistent with these findings, immunohistochemical (IHC) staining revealed stronger MCT4 and pan-Kla signals in tumor tissues from nonresponders, along with decreased $CD8^+$ T-cell infiltration (Figure 2E-I). Together, these results support the notion that excessive glycolysis and lactate export through MCT4 may contribute to an immunosuppressive tumor microenvironment and resistance to immunotherapy.

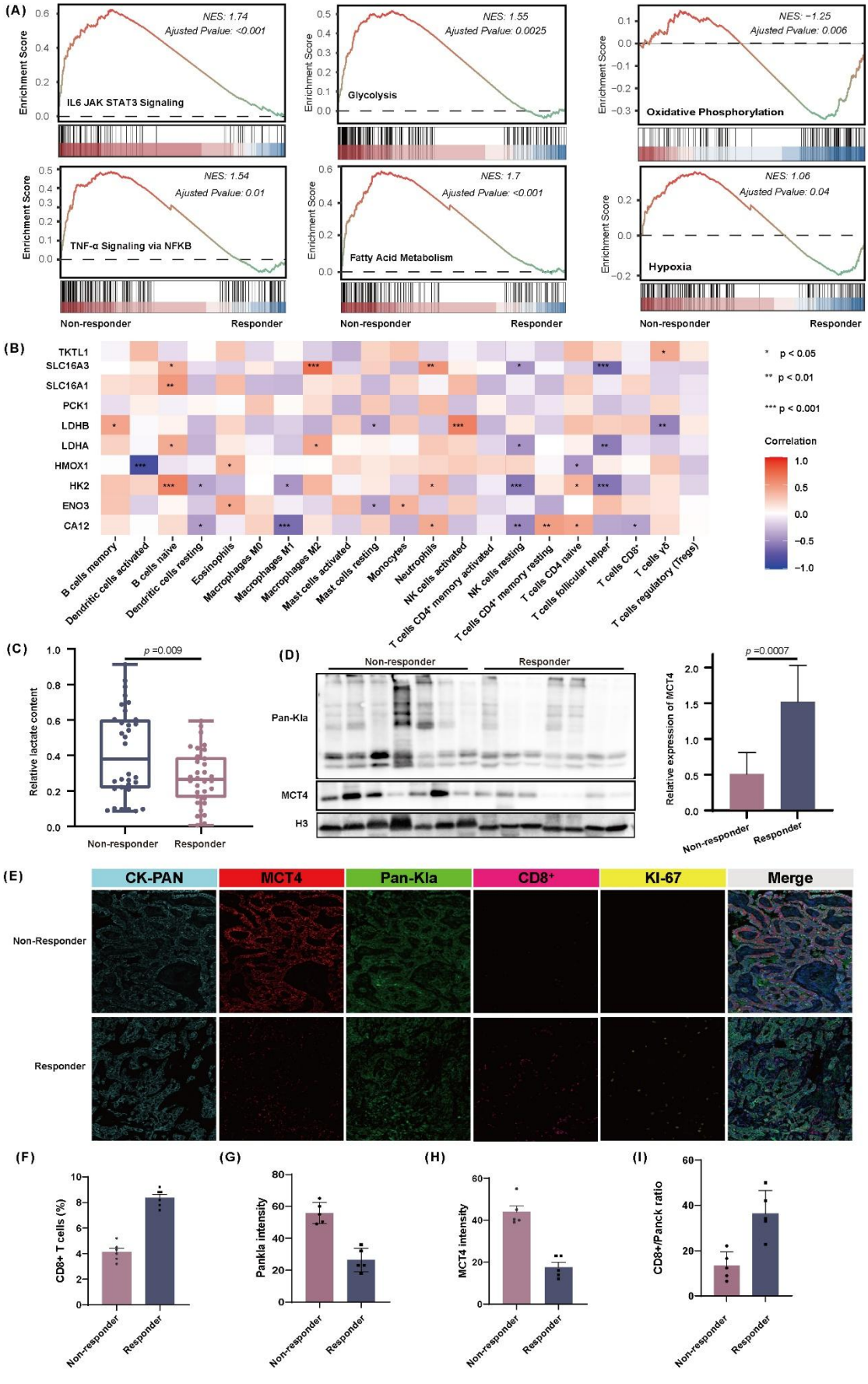

Figure 2. In nonresponder lesions, glycolysis is activated and the expression of MCT4 and Pan-Kla is increased. (A) GSEA of transcriptomic data from ICB responder and nonresponder patients revealed pathway-level differences. (B) Correlations between immune cell populations and the expression of glycolysis pathway-related genes. (C) Quantification of lactate concentrations in NSCLC tissues from ICB responder and nonresponder patients (n = 32). (D) Immunoblot analysis of pan-Kla and MCT4 expression in NSCLC tissues from responders (n = 7) and nonresponders (n = 7). (E) Representative immunofluorescence staining images of the tumor tissues from patients after immunotherapy (5 nonresponders and 5 responders) for pan-Kla/MCT4/$CD8^+$/KI-67/CK-PAN. Scale bars, 50 μm. (F-I) The numbers of CD8+ T cells and the PKla and MCT4 expression levels were analyzed in tissues from nonresponders and responders.

2.3 MCT4 deficiency promotes the alleviation of $CD8^+$ T-cell dysfunction by impairing lactate secretion

To further investigate the transcriptional and proteomic features associated with the nonresponse to immune checkpoint blockade (ICB) in our clinical cohort, we examined tumor-intrinsic properties using a preclinical murine model of ICB resistance. Like anti-PD-1-responsive lung cancers, MC38 and LLC tumor models serve as well-established preclinical systems for studying tumor-intrinsic determinants of sensitivity and resistance to ICB therapy [7]. As expected, subcutaneous MC38 tumors exhibited a marked reduction in tumor volume after three consecutive doses of the anti-PD-1 antibody, whereas the LLC tumors displayed only a minimal response (Figure 3A). We next compared lactate levels and protein lactylation among normal lung fibroblasts (MRC-5), anti-PD-1-sensitive MC38 cells, and anti-PD-1-refractory LLC cells. Measurements of intracellular and extracellular lactate levels revealed markedly higher lactate concentrations in LLC cells than in MC38 cells (Figure 3B). Consistently, Western blot analysis revealed that compared with those in MC38 and MRC5 cells, both pan-Kla and MCT4 expression levels were elevated in LLC cells (Figure 3C). Moreover, the immune profiles of the tumors were evaluated using flow cytometry. The results revealed the presence of exhausted $CD8^+$ T cells and associated Granzyme B secretion in subcutaneous tumors derived from LLC cells (Figure 3D). These results are consistent with our clinical findings that tumor cells that are resistant to immunotherapy may establish an immunosuppressive microenvironment through MCT4-mediated lactate secretion, thereby impairing $CD8^+$ T-cell proliferation and effector functions and ultimately leading to a diminished response to ICB. To explore the functional role of MCT4 in tumor resistance to ICB, we used CRISPR/Cas9 gene editing to knockout the *MCT4* gene (*MCT4*-KO) in LLC cells (Figure 3E and 3F). Consistent with its role in lactate transport, *MCT4* depletion resulted in decreased extracellular lactate levels and an increase in the intracellular accumulation of lactate (Figure 3G). To further examine the effect of *MCT4* deficiency-mediated lactate export secretion on $CD8^+$ T cells, we conducted *in vitro* cytotoxicity studies (Figure 3H). $CD8^+$ T cells isolated from C57BL/6 mouse spleens were cocultured with WT and *MCT4*-KO cells at a 33:1 effector-to-target (E:T) ratio. We found that pan-Kla levels were markedly elevated in $CD8^+$ T cells cocultured with LLC cells and

that this increase was mitigated by *MCT4* knockout (Figure 3H). Furthermore, coculture of $CD8^+$ T cells with LLC cells markedly reduced their proliferative capacity and production of IFN-γ and Granzyme B, whereas these suppressive effects were alleviated when *MCT4* was knocked out (Figure 3I). To investigate whether lactate directly affects $CD8^+$ T cells, we stimulated CTLL-2 and primary $CD8^+$ T cells with different concentrations of lactate. The results revealed that increasing lactate concentrations led to elevated protein lactylation in $CD8^+$ T cells (Figure S3A and S3B), which was accompanied by reduced proliferation and diminished effector cytokine production (IFN-γ and Granzyme B) (Figure S3C and S3D). Collectively, these findings confirm that elevated *MCT4*-mediated lactate secretion from tumor cells dampens $CD8^+$ T-cell proliferation and effector activity.

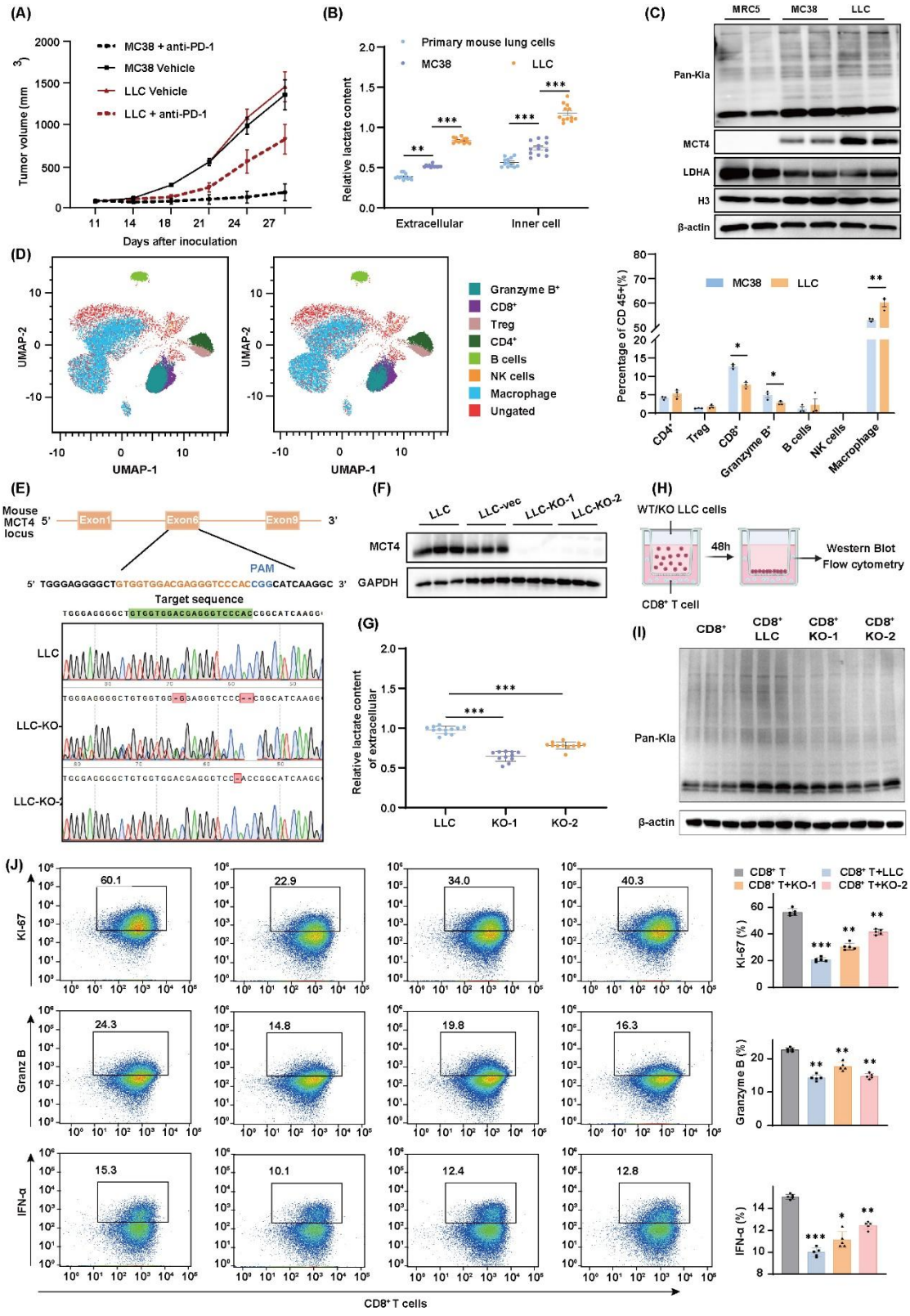

Figure 3. MCT4 knockout impairs lactate export and alleviates CD8⁺ T-cell dysfunction. (A) Growth of MC38 and LLC subcutaneous tumors in C57BL/6 mice that were treated with PBS or an anti-PD-1 antibody. (B) Intracellular and extracellular lactate levels were detected using a colorimetric method in MRC5, MC38 and LLC cells. (C) Pan-Kla and MCT4 protein levels in MRC5, MC38 and LLC cells were measured by Western blotting. (D) The immune cell profiles of MC38 and LLC subcutaneous tumors

treated with anti-PD-1 antibodies were assessed by flow cytometry. (E) Gene targeting strategy for generating MCT4-knockout LLC cells. DNA sequence analysis revealed the presence of the MCT4 frameshift mutation in LLC cells. (F) Western blot analysis confirmed the knockout efficiency of the MCT4 protein in LLC cells. (G) Extracellular lactate levels in *MCT4-KO* cells. (H-I) Western blot analysis of pan-Kla levels in $CD8^+$ T cells cocultured with LLC WT and *MCT4-KO* cells. (J) Flow cytometric analysis of Ki-67, IFN-γ, and Granzyme B expression in $CD8^+$ T cells after coculture with LLC WT and *MCT4-KO* cells.

2.4 Knockout of MCT4 perturbs metabolic mitochondrial activity and cell cycle regulation in LLC cells

Recent studies have indicated that knockout of MCT4 impairs lactate secretion from and the viability of LKB1-deficient cells [13]. However, in our LLC *MCT4*-KO cell model, Annexin V/PI double staining revealed no significant difference in apoptosis between LLC WT and *MCT4*-KO1/2 cells (Figure S4A–S4C), but CCK-8 assays demonstrated a marked difference in their proliferative capacity (Figure S4D). To elucidate the molecular mechanisms underlying these phenotypic changes, we performed integrated proteomic and phosphoproteomic analyses of LLC WT and *MCT4*-KO1/2 cells. In total, 4625 proteins and 2482 phosphoproteins were identified, with 993 proteins detected only after phosphorylation enrichment (Figure 4A). Among the phosphosites, phosphoserine (pS), phosphothreonine (pT), and phosphotyrosine (pY) accounted for 80.54%, 16.73%, and 2.73%, respectively (Figure 4B), confirming the high specificity of Ti^{4+}-IMAC enrichment. The phosphorylation enrichment efficiency with Ti^{4+}-IMAC was 98.1%, with 90.72% of the phosphosites derived from phosphoserine (pS), 8.9% derived from phosphorylated threonine (pT) and 0.38% derived from phosphorylated tyrosine (pY). Compared with those in the LLC CTRL cells, a total of 261 proteins were significantly upregulated and 372 were downregulated in both *MCT4*-KO-1 and -KO-2 cells (FC ≥ 2 or ≤ 0.5; $p < 0.05$) (Figure 4C). Similarly, 114 phosphoproteins were significantly upregulated and 242 were downregulated in both *MCT4* KO-1 and KO-2 cells (Figure 4D). These differentially expressed proteins and phosphoproteins were subjected to clustering and functional analyses (Figure 4E and Figure S4F-4G). GO and KEGG analyses revealed that these differentially expressed proteins are involved in functions such as mitochondrial protein degradation, oxidative phosphorylation, and cell cycle checkpoints. Furthermore, Ywhah, Ywhag and Ywhae are involved in the modulation of various functions. As shown in the heatmap, the Ywhah, Ywhag and Ywhae protein levels decreased 6.6-fold, 7.8-fold and 4.1-fold, respectively, in the *MCT4*-KO cells. We next inferred kinase activity on the basis of the substrate phosphorylation levels and the corresponding kinase-activating sites. Phosphosite-specific signature enrichment analysis (PTM-SEA) revealed 12 kinases in *MCT4*-KO cells (Figure 4F), among which the expression of 5 kinases, namely, Chk1, Mapk1, Cdk1, Gsk3a, and Src, increased (Figure 4G). Moreover, these kinases exhibited greater changes upon comparison of the KO and WT cells in terms of phosphosite abundance than in terms of protein abundance. Specifically, cyclin-dependent kinase 1 (Cdk1) is a key player that controls the cell cycle [34] and regulates the transition between

the G2 phase and mitosis [35]. We found that the levels of the Cdk1 protein and its T161 phosphosite were increased in KO cells, which was accompanied by increased expression of substrates involved in the cell cycle and cell signaling regulation, such as Lmna S390, Efhd2 S74, Wwtr1 S90, and Rrm2 S20 (Figure 4H).

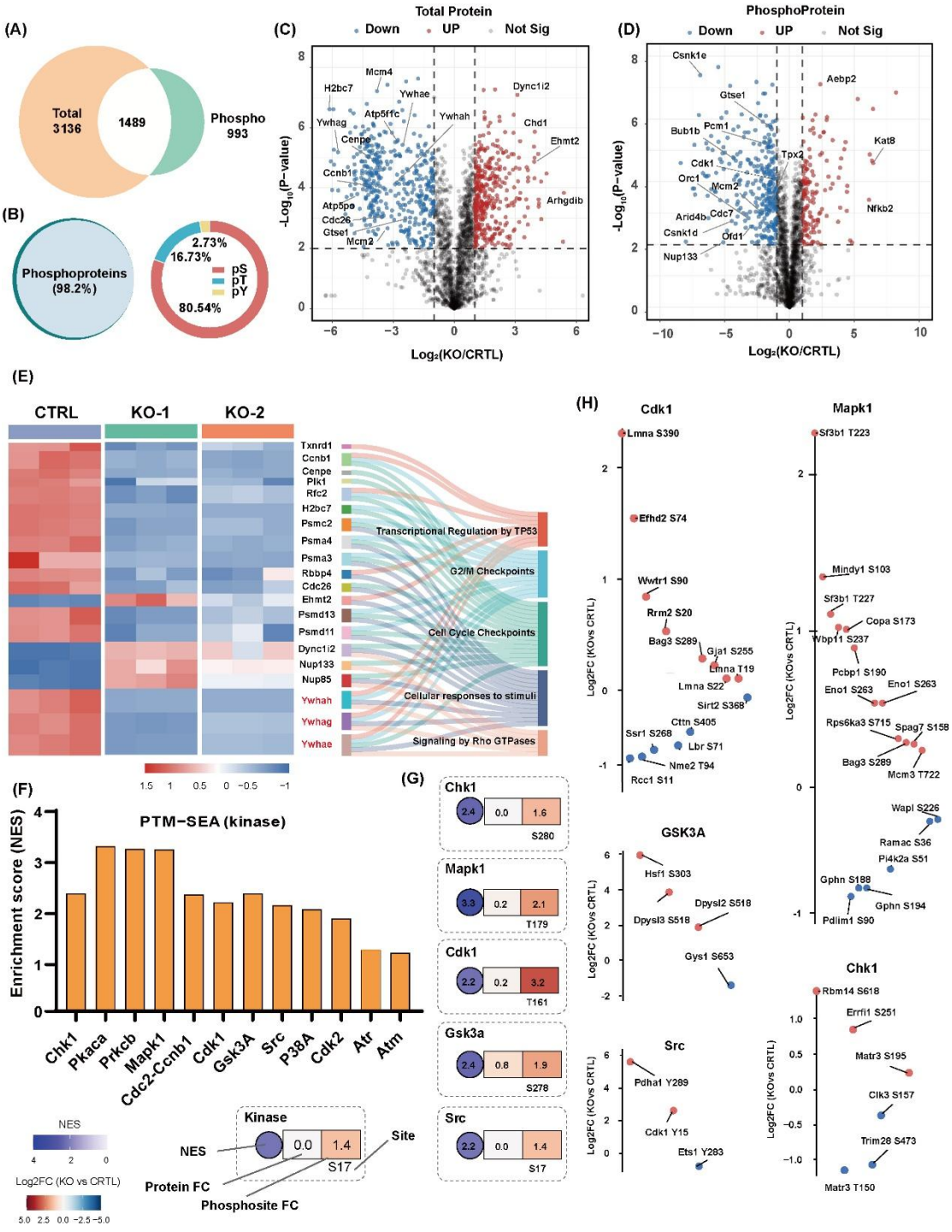

Figure 4 Effects of *MCT4* knockout on total and phosphorylated protein levels. (A) Venn diagrams showing the identified total and phosphorylated proteins in LLC and LLC *MCT4*-ko cells. (B) Specificity of the phosphorylated proteins isolated by Ti^{4+}-IMAC and the proportions of phosphoserine (pS), phosphothreonine (pT), and phosphotyrosine (pY) residues among the phosphosites. Volcano plot representing the results of the quantitative analysis of LLC MCT4-KO1/2 cells versus CTRL cells in terms

of (C) total protein and (D) phosphoprotein levels. (E) Hierarchical clustering heatmap and functional enrichment analysis of differentially expressed proteins in MCT4-depleted LLC cells. (F) Kinase signatures were significantly (FDR < 0.05) different between MCT4-KO1/2 LLC cells and control LLC cells, as assessed by PTM signature enrichment analysis (PTM-SEA). (G) Diagram showing kinases with increased activity inferred from the phosphorylation levels of their substrates and the corresponding kinase-activating sites. (H) Dot plot showing the median $\log_2$-fold change in kinase substrate phosphorylation. Pink and blue indicate sites with increased and decreased phosphorylation, respectively, between LLC WT and *MCT4-ko* cells.

We next examined the effects of *MCT4* depletion on the cell cycle, and as expected, flow cytometry analysis revealed that the proportion of cells in the G2/M phase was significantly greater in both *MCT4*-KO1 and KO2 cells than in LLC-WT cells, indicating cell cycle arrest (Figure 5A). Furthermore, proteomic analysis revealed significant enrichment of pathways, such as mitochondrial protein degradation, the citrate cycle and oxidative phosphorylation. Mitochondria are the primary site of cellular energy production and are responsible for generating ATP through oxidative phosphorylation and coordinating key metabolic pathways such as the TCA cycle [36]. On the basis of the above findings, we investigated whether *MCT4* regulates mitochondrial function. DCFH-DA fluorescence assays revealed elevated intracellular reactive oxygen species (ROS) levels in *MCT4*-KO1 and KO2 cells (Figure 5B), whereas intracellular ATP concentrations were markedly reduced (Figure 5C), suggesting impaired mitochondrial energy metabolism. Fluorescence microscopy of JC-1-stained cells revealed that *MCT4* knockout significantly reduced the mitochondrial membrane potential (MMP), providing additional evidence that *MCT4* deficiency is involved in the regulation of mitochondrial homeostasis (Figure 5D).

Given the increased oxidative stress and compromised mitochondrial membrane potential detected in *MCT4*-deficient cells, we next assessed whether the mitochondrial content was altered as an adaptive response. Mitochondrial homeostasis relies on the dynamic balance between mitochondrial biogenesis and mitophagy [37]. Mitochondrial DNA (mtDNA) copy number, which reflects the relative abundance of mitochondrial genomes, is widely used as a surrogate indicator of mitochondrial content and functional status [38]. Notably, MCT4 knockout resulted in a significant increase in mtDNA copy number (Figure 5E), which suggests that mtDNA amplification may represent a compensatory, self-protective response of tumor cells to mitochondrial stress, potentially functioning to preserve mitochondrial integrity and limit apoptosis [39]. To determine whether the mitochondrial defects observed upon MCT4 depletion were directly attributable to the loss of MCT4 activity, we next assessed the impact of pharmacological MCT4 inhibition on mitochondrial function. We first treated LLC cells with increasing concentrations of an MCT4 inhibitor (HY-148517) for 24 and 48 hours to evaluate its effect on lactate transport activity. Quantification of extracellular and intracellular lactate revealed a dose-dependent reduction following 24 h and 48 h of MCT4 inhibition (Figure 5F-5G). Notably, treatment with the MCT4 inhibitor at a concentration of 80 nM for 48 hours resulted in a significant decrease in extracellular lactate levels, indicating effective suppression of MCT4-mediated lactate export. Treatment of LLC cells with the MCT4 inhibitor markedly increased intracellular ROS levels, concomitant with a significant reduction in the

intracellular ATP content (Figure 5H–5I). Moreover, compared with control cells, MCT4 inhibitor-treated cells exhibited a pronounced increase in mitochondrial DNA (mtDNA) copy number (Figure 5J), accompanied by a significant decrease in mitochondrial membrane potential, as assessed by JC-1 staining (Figure 5K). Collectively, these findings demonstrate that inhibition of MCT4 activity is sufficient to impair mitochondrial function and trigger mitochondrial stress responses.

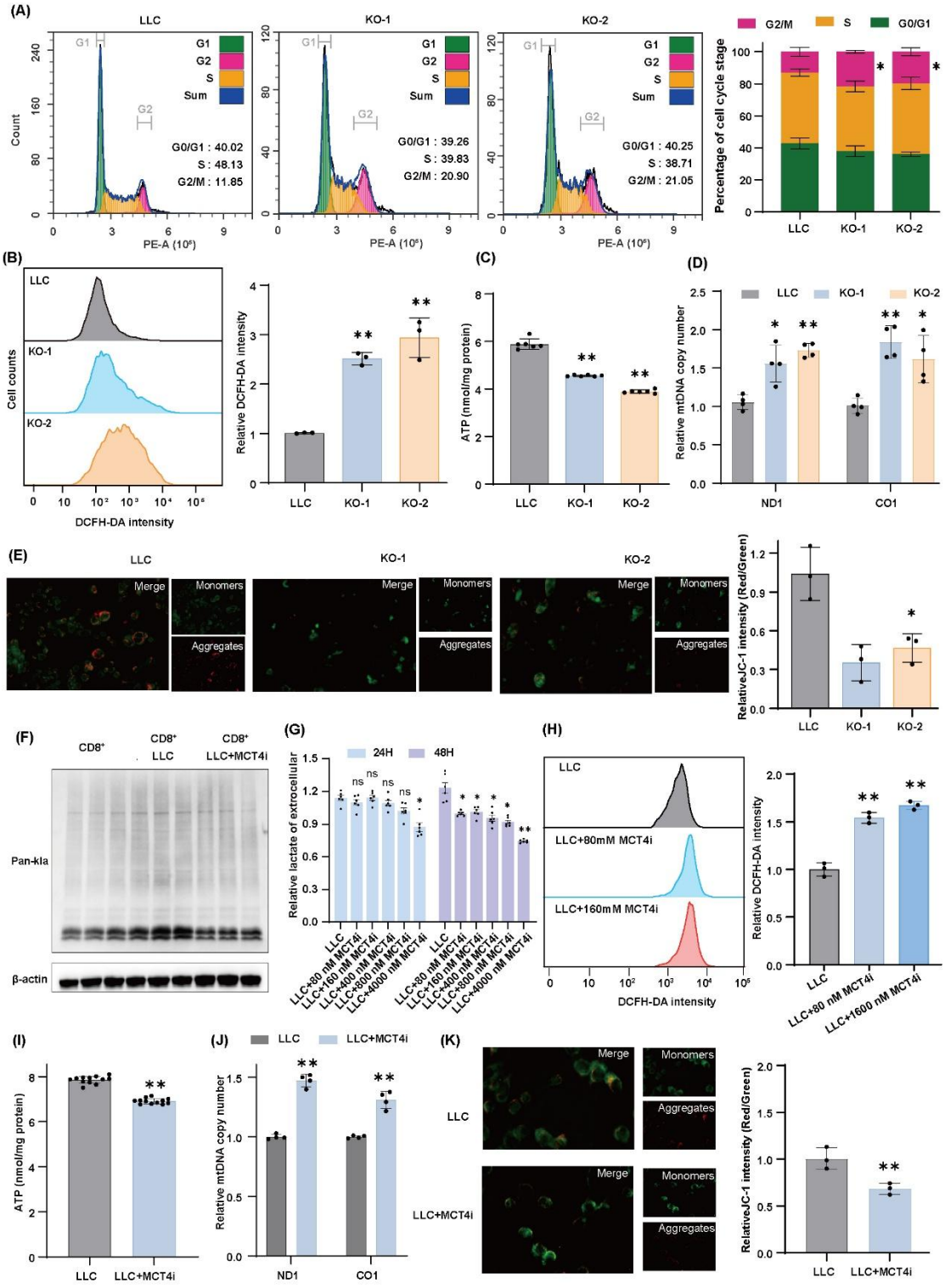

Figure 5 MCT4 perturbs mitochondrial dysfunction and cell cycle regulation. (A) Flow cytometry analysis of the cell cycle in LLC and LLC *MCT4*-ko cells. The percentages of cells in G0/G1, S and G2/M are shown as stacked bar plots. (B) The levels of intracellular ROS were investigated by flow cytometry in LLC and LLC *MCT4*-ko cells. (C) Measurement of ATP levels in LLC and LLC *MCT4*-ko cells. (D) Relative mtDNA content in LLC and LLC *MCT4*-ko cells. The levels of MT-ND1 and MT-CO1, normalized to that of β2-microglobulin (β2-MG), were used as measures of the mtDNA copy number. (E) Representative fluorescence images of JC-1 staining in LLC and LLC *MCT4*-ko cells. Red fluorescence represents JC-1 aggregates, and green fluorescence represents JC-1 monomers. (F) Extracellular lactate contents after LLC cells were treated with different concentrations of MCT4 inhibitors for 24 hours or 48 hours. (G) Western blot analysis of pan-Kla levels in $CD8^+$ T cells cocultured with LLC cells and LLC cells treated with the MCT4 inhibitor. (H) The levels of intracellular ROS were investigated by flow cytometry in LLC and LLC cells treated with the MCT4 inhibitor. (I) Measurement of ATP levels in LLC and LLC cells treated with the MCT4 inhibitor. (J) Relative mtDNA content in LLC and LLC cells treated with the MCT4 inhibitor. (K) Representative fluorescence images of JC-1 staining in LLC and LLC cells treated with the MCT4 inhibitor.

2.5 MCT4 orchestrates cell cycle arrest through EHMT2/H3K9me3 epigenetic regulation

To further elucidate the molecular mechanism underlying MCT4 deficiency-induced G2/M cell cycle arrest, we performed pathway enrichment analysis on the basis of quantitative proteomic profiles of WT and MCT4-KO cells. Notably, proteins involved in chromatin-modifying enzyme pathways were among the most significantly altered in MCT4-KO cells (Figures S4G, S6A). A heatmap of the proteins in these pathways revealed marked upregulation of the histone methyltransferase EHMT2 (Figure S6B-S6C). Consistent with the proteomic data, EHMT2 protein levels were significantly elevated in MCT4-KO cells compared with those in WT cells, as determined by western blotting (Figure 6A). Given that EHMT2 functions as a key enzyme responsible for histone H3 lysine 9 methylation, we subsequently examined whether MCT4 deficiency affects global H3K9 methylation status. Indeed, H3K9me3 levels were markedly increased in MCT4-KO cells (Figure 6A), suggesting the activation of an EHMT2/H3K9me3-dependent epigenetic program upon MCT4 loss.

H3K9 methylation is directly associated with transcriptional silencing. To identify the downstream genes regulated by H3K9me3, we conducted CUT&Tag H3K9me3 profiling in WT and MCT4-KO NSCLC cells (Figure 6B). H3K9la occurs near the transcription start sites (TSSs) of most genes. The intensity of the H3K9me3 enrichment peak was significantly greater in MCT4-KO cells than in WT cells (Figure 6C). Peak distribution analysis revealed that 22.72% and 26.97% of the differential H3K9me3 binding peaks in the WT and MCT4-KO cell lines, respectively, were located within the promoter region (Figure 6D). To determine the consequence of H3K9me3-mediated regulation, we analyzed the enrichment of genes at the binding sites using KEGG and GO analyses. The candidate pathways included the Wnt, p53, mTOR, Hippo, and ErbB signaling pathways (Figure 6E and Figure S6C), which are involved in cell cycle progression, cellular

proliferation, and tumorigenesis. We next focused on identifying H3K9me3-regulated genes with potential roles in cell cycle control. Integrated analysis of the CUT&Tag data revealed several cell cycle-associated genes that were significantly upregulated in MCT4-KO cells, including Hjurp, Fzr1, Fbxo5, Cdt1, Fzd8, and Wls (Figure 6F–G and Figure S6E). To determine whether these genes were directly regulated by H3K9me3, we performed ChIP–qPCR assays targeting their promoter regions. Among the six candidate genes, Hjurp, Fzr1, Fbxo5, and Cdt1 exhibited significantly increased H3K9me3 occupancy at their promoters in MCT4-KO cells compared with WT cells (Figure 6H), indicating that these genes represent direct downstream targets of EHMT2-mediated H3K9me3 regulation.

Finally, to assess whether EHMT2/H3K9me3 could also be activated by MCT4 inhibition, we treated cells with an MCT4 inhibitor and evaluated the levels of EHMT2 and H3K9me3. MCT4 inhibitor treatment resulted in marked increases in EHMT2 and H3K9me3 levels (Figure 6I). Moreover, ChIP–qPCR analysis confirmed increased H3K9me3 enrichment at the promoters of key cell cycle-related genes, including Fzr1, Fbxo5, Cdt1, and Wls, further supporting a central role for the MCT4–EHMT2/H3K9me3 epigenetic axis in cell cycle arrest regulation.

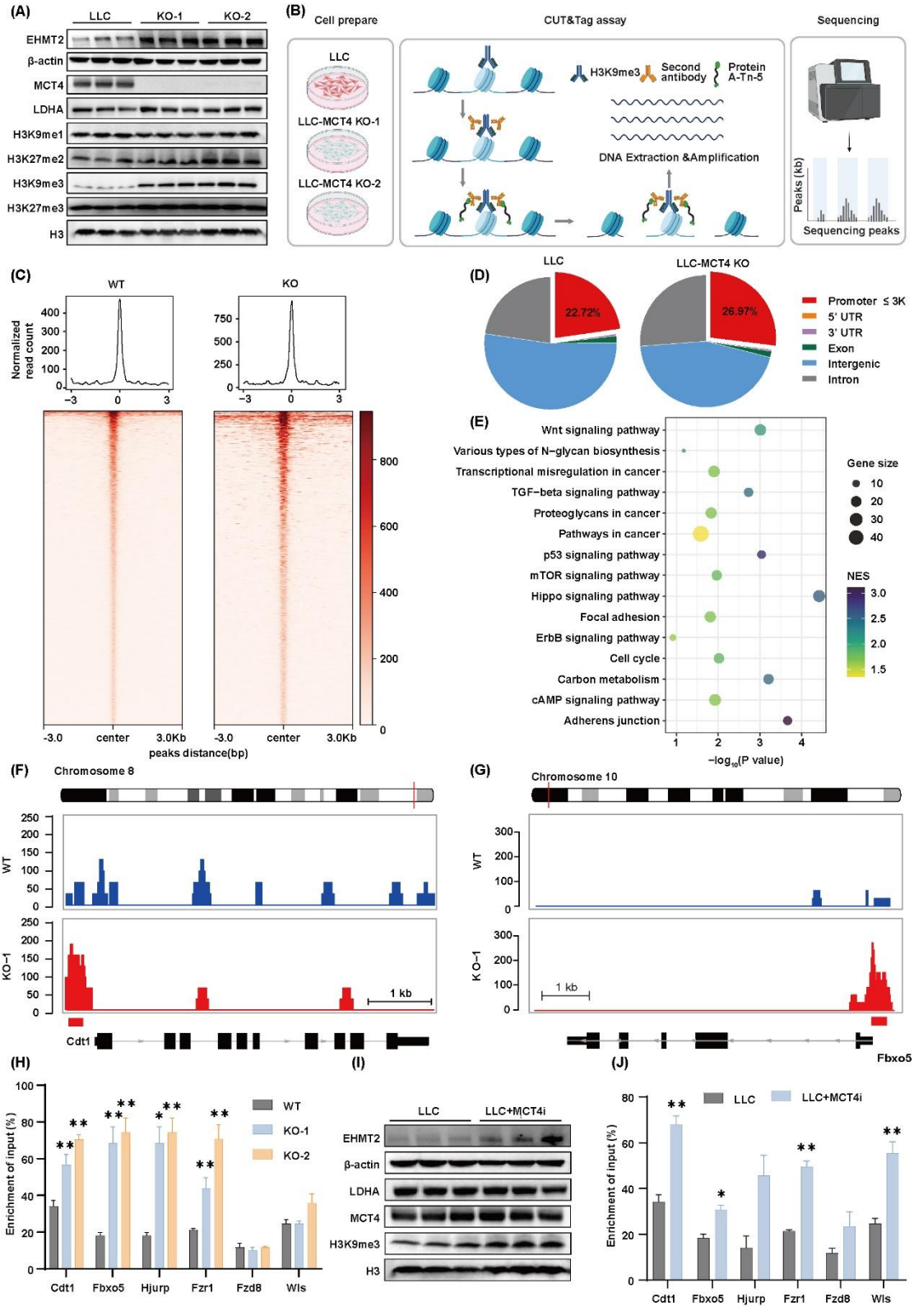

Figure 6 H3K9me3-mediated epigenetic silencing of cell cycle regulatory genes in MCT4-deficient NSCLC cells. (A) EHMT2 and H3 methylation levels were detected in WT and MCT4-KO cells. (B) Brief scheme of the cell processing and CUT&Tag-seq procedures. (C) TSS heatmap showing the binding density of H3K9me3 in WT and MCT4-KO cells. (D) Genome-wide distribution of the differential H3K9me3-binding peaks. (E) KEGG enrichment analysis of the increased peaks upon the binding of

H3K9me3 to the candidate genes. Genome browser track analysis shows the H3K9me3 levels in the (F) Cdt1 and (G) Hjurp binding regions in WT and MCT4-KO cells. (H) The promoters of the candidate genes that bind to H3K9me3 in WT and MCT4-KO cells were detected using ChIP–qPCR. (I) EHMT2 and H3 methylation levels were detected after culture in the absence and presence of the MCT4 inhibitor (80 nM). (J) The promoters of the candidate genes that bind to H3K9me3 after treatment without or with 80 nM MCT4 inhibitor were detected using ChIP–qPCR.

2.6 MCT4 loss increases the efficacy of immune checkpoint blockade therapy in highly glycolytic tumors

The aforementioned data provide evidence that increased glycolysis promotes increased lactate secretion via MCT4 and that this lactate-MCT4 pathway affects both $CD8^+$ T-cell function and tumor-intrinsic programs. To directly assess the impact of MCT4 loss on tumor growth and immunotherapy responsiveness *in vivo*, LLC WT and MCT4-KO cells were subcutaneously implanted into C57BL/6J mice (Figure 7A). While MCT4 deficiency alone moderately restrained tumor progression, compared with control tumors, MCT4-KO tumors a markedly increased response to anti-PD-1 treatment, resulting in significantly reduced tumor growth (Figure 7B). MCT4-KO tumors treated with anti–PD-1 antibodies displayed a significantly increased percentage of proliferating $CD8^+$ T cells (Figure 7C). Flow cytometric analysis of tumor-infiltrating lymphocytes further demonstrated that these $CD8^+$ T cells exhibited increased proliferation and effector function, as evidenced by increased production of Ki-67 and IFN-γ (Figure 7D).

Next, we evaluated the therapeutic efficacy of MCT4 inhibition combined with PD-1 blockade in a high-glycolysis tumor model. Compared with anti-PD-1 monotherapy, coadministration of the MCT4 inhibitor significantly suppressed tumor growth, resulting in markedly reduced tumor volume (Figure 7F). Compared with either the control or anti-PD-1 antibody-treated tumors, the combination treatment led to a higher percentage of tumor-infiltrating $CD8^+$ T cells (Figure 7G). Flow cytometric analysis revealed that combined MCT4 inhibition and PD-1 blockade synergistically increased the proportion of proliferating $CD8^+$ cytotoxic T lymphocytes, as indicated by elevated Ki-67 expression (Figure 7H). In parallel, compared with anti-PD-1 antibody-treated tumors, $CD8^+$ T cells from tumors after combination treatment exhibited reduced expression of inhibitory receptors, including TIM-3, PD-1, and LAG-3 (Figure 7H). Together, these data indicate that MCT4 inhibition increases the antitumor efficacy of PD-1 blockade by promoting $CD8^+$ T-cell expansion while partially alleviating exhaustion-associated phenotypes within the tumor microenvironment.

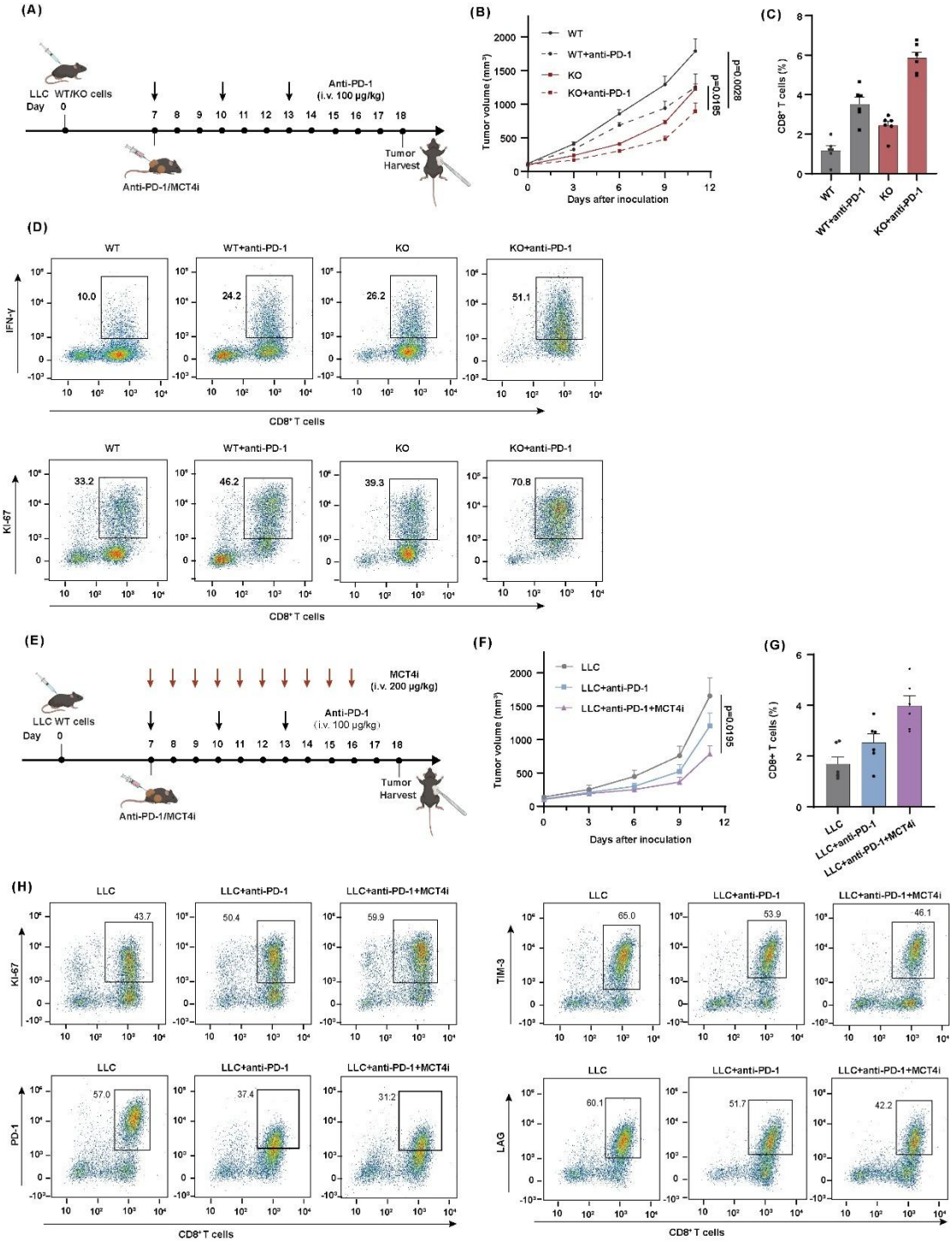

Figure 7 MCT4 knockout impairs tumor growth and increases the response to immunotherapy in highly glycolytic tumors. (A) LLC cells with or without MCT4 KO were injected into C57BL6/J mice, which were then treated with PBS or an anti-PD-1 antibody every third day. (B) Tumor growth curves and changes in volume in the different groups. (C) Percentages of $CD8^+$ T cells in the different groups. (D) Flow cytometric analysis of IFN-γ and Ki-67 expression in tumor-infiltrating $CD8^+$ T cells from different groups. (E) LLC cells treated with an anti-PD1 antibody or the combination of an anti-PD-1 antibody and the MCT4 inhibitor. (F) Tumor growth curves and changes in volume in the different groups. (G) Percentages of $CD8^+$ T cells in the different groups. (H) Flow cytometric analysis of Ki-67, TIM-3, PD-1, and LAG-3 expression in tumor-infiltrating $CD8^+$ T cells from different groups.

Discussion

Immunotherapies targeting PD-1 have been approved as first-line therapies for NSCLC, but a large proportion of patients still show primary resistance [5-7], emphasizing the need to formulate rational combination therapies. Accumulating evidence suggests that tumor-intrinsic metabolic reprogramming is a critical but incompletely understood determinant of immune evasion and resistance to immune checkpoint blockade [11, 12]. In this study, through integrated transcriptomic and proteomic analyses of clinical samples from responders and nonresponders, we demonstrated that nonresponder tumors undergo metabolic reprogramming characterized by the activation of glycolysis and increased expression of MCT4. Nonresponsive patients with solid tumors may exhibit a distinct “cold” phenotype [40]. Several studies have reported that MCT4-dependent lactate secretion is a mediator of this “cold” immune phenotype, especially in LUAD patients with STK11/LKB1 alterations [41]. We compared MC38 and LLC cells, which display different sensitivity to anti-PD-1 therapy. Despite comparable LDHA expression, LLC cells presented substantially higher lactate and MCT4 expression levels than MC38 cells did, indicating that increased MCT4-mediated lactate secretion is a potential contributor to immunotherapy resistance.

Given the known immunosuppressive effects of lactate [29, 42], we next investigated the role of the MCT4/lactate axis in resistance to ICB. We generated an LLC M*CT4-KO* cell line. In contrast to the findings reported by Heymach *et al*. [13], who demonstrated that MCT4 deletion impaired lactate secretion and compromised cell viability, MCT4 knockout in LLC cells resulted primarily in profound mitochondrial dysfunction, which was characterized by increased reactive oxygen species accumulation, reduced ATP production, loss of mitochondrial membrane potential, and a compensatory increase in mitochondrial DNA copy number. Notably, these mitochondrial perturbations did not culminate in apoptotic cell death; instead, they triggered G2/M cell cycle arrest, indicating an adaptive stress response rather than terminal cytotoxicity. Mechanistically, we revealed that MCT4 deficiency activates an EHMT2-mediated H3K9me3 epigenetic program that directly governs cell cycle regulation. Subsequent CUT&Tag and ChIP–qPCR analyses demonstrated widespread redistribution of H3K9me3 at promoter regions of genes involved in controlling cell cycle licensing and mitotic progression, including Hjurp, Fzr1, Fbxo5, and Cdt1.

At the level of the tumor immune microenvironment, our study revealed that MCT4-dependent lactate secretion simultaneously impaired $CD8^+$ T-cell function and limited the efficacy of PD-1 blockade. In both *in vitro* coculture systems and *in vivo* tumor models, MCT4 deficiency alleviated the lactate-induced suppression of $CD8^+$ T-cell proliferation and effector cytokine production. These findings substantially expand the current paradigm of lactate-mediated epigenetic regulation in cancer. Previous studies have largely focused on histone lactylation as an activating epigenetic modification that promotes transcriptional programs associated with immune suppression and tumor progression. In contrast, our work demonstrates that lactate metabolism can also engage in repressive chromatin mechanisms, specifically through EHMT2/H3K9 trimethylation.

This dual capacity highlights lactylation as a versatile metabolic signal capable of modulating chromatin states in a context-dependent manner, thereby coordinating both the intrinsic fate decisions of tumor cells and their immune interactions under therapeutic pressure.

MCT4 is associated with the export of lactic acid from cancer cells under hypoxia; thus, it is a target of interest for oncology, and inhibition of MCT4 has the potential to increase the antitumor efficacy of immunomodulatory agents [33]. Critchlow *et al*. reported that the MCT4 inhibitor AZD0095 had excellent antitumor efficacy when combined with a VEGFR inhibitor [43]. Here, we demonstrate that AZD0095 effectively suppresses lactate secretion from LLC cells and induces mitochondrial dysfunction. This metabolic disruption consequently perturbs the epigenetic activity of EHMT2/H3K9me3, leading to G2/M cell cycle arrest. Notably, the combination of an MCT4 inhibitor with anti-PD-1 therapy markedly suppressed tumor growth in LLC tumor-bearing mice, highlighting the therapeutic potential of targeting the MCT4/lactate pathway to overcome immune resistance.

In summary, our study identifies MCT4 as a metabolic–epigenetic immune checkpoint that integrates tumor glycolysis, chromatin repression, and antitumor immunity. By linking lactate export to EHMT2-mediated epigenetic reprogramming and immune dysfunction, we provide a mechanistic framework explaining how highly glycolytic tumors evade immune surveillance and resist PD-1 blockade. These findings offer a compelling rationale for combining therapeutic strategies targeting tumor metabolism and immune checkpoints to overcome immunotherapy resistance in NSCLC patients.

Declarations

Competing interests

The authors declare that they have no competing financial interests.

Funding

This study was supported by guiding grants from the Central Government for Supporting the Development of the Local Science and Technology (2024ZY01013), and the China Postdoctoral Science Foundation (2025M782779).

Acknowledgment

Not applicable.

Authors' contributions

S.H. and H.Y.W contributed to the study design. The manuscript was written by H.Y.W., S.H., X.M.N. and H.X. All the authors reviewed the manuscript.

Reference

1. Bray, F., M. Laversanne, H. Sung, et al., Global Cancer Statistics 2022: Globocan Estimates of Incidence and Mortality Worldwide for 36 Cancers in 185 Countries. ***CA: a cancer journal for clinicians*** 2024, **74**(3): 229-263.
2. Hendriks, L.E.L., J. Remon, C. Faivre-Finn, et al., Non-Small-Cell Lung Cancer. ***Nature Reviews Disease Primers*** 2024, **10**(1): 71.
3. Bian, D., L. Sun, J. Hu, et al., Neoadjuvant Afatinib for Stage Iii Egfr-Mutant Non-Small Cell Lung Cancer: A Phase Ii Study. ***Nature Communications*** 2023, **14**(1): 4655.
4. Lu, S., W. Zhang, L. Wu, et al., Perioperative Toripalimab Plus Chemotherapy for Patients with Resectable Non-Small Cell Lung Cancer: The Neotorch Randomized Clinical Trial. ***Jama*** 2024, **331**(3): 201-211.
5. Reck, M., N. Frost, S. Peters, et al., Treatment of Nsclc after Chemoimmunotherapy — Are We Making Headway? ***Nature Reviews Clinical Oncology*** 2025, **22**(11): 806-830.
6. Yan, Y., D. Sun, J. Hu, et al., Multi-Omic Profiling Highlights Factors Associated with Resistance to Immuno-Chemotherapy in Non-Small-Cell Lung Cancer. ***Nature Genetics*** 2025, **57**(1): 126-139.
7. Memon, D., A.J. Schoenfeld, D. Ye, et al., Clinical and Molecular Features of Acquired Resistance to Immunotherapy in Non-Small Cell Lung Cancer. ***Cancer Cell*** 2024, **42**(2): 209-224.e9.
8. Zhang, C., L. Zhou, M. Zhang, et al., H3k18 Lactylation Potentiates Immune Escape of Non-Small Cell Lung Cancer. ***Cancer research*** 2024, **84**(21): 3589-3601.
9. Wang, R., C. Li, Z. Cheng, et al., H3k9 Lactylation in Malignant Cells Facilitates Cd8(+) T cell Dysfunction and Poor Immunotherapy Response. ***Cell reports*** 2024, **43**(9): 114686.
10. Yang, Z., C. Yan, J. Ma, et al., Lactylome Analysis Suggests Lactylation-Dependent Mechanisms of Metabolic Adaptation in Hepatocellular Carcinoma. ***Nature Metabolism*** 2023, **5**(1): 61-79.
11. Wang, J., M. Peng, L. Oyang, et al., Mechanism and Application of Lactylation in Cancers. ***Cell & Bioscience*** 2025, **15**(1): 76.
12. Kao, K.-C., S. Vilbois, C.-H. Tsai, et al., Metabolic Communication in the Tumour–Immune Microenvironment. ***Nature Cell Biology*** 2022, **24**(11): 1574-1583.
13. Qian, Y., A. Galan-Cobo, I. Guijarro, et al., Mct4-Dependent Lactate Secretion Suppresses Antitumor Immunity in Lkb1-Deficient Lung Adenocarcinoma. ***Cancer Cell*** 2023, **41**(7): 1363-1380.e7.

14. Javaeed, A. and S.K. Ghauri, Mct4 Has a Potential to Be Used as a Prognostic Biomarker - a Systematic Review and Meta-Analysis. ***Oncology reviews*** 2019, **13**(2): 403.
15. Zhang, D., Z. Tang, H. Huang, et al., Metabolic Regulation of Gene Expression by Histone Lactylation. ***Nature*** 2019, **574**(7779): 575-580.
16. Ren, H., Y. Tang, and D. Zhang, The Emerging Role of Protein L-Lactylation in Metabolic Regulation and Cell Signalling. ***Nature Metabolism*** 2025, **7**(4): 647-664.
17. Eisenhauer, E.A., P. Therasse, J. Bogaerts, et al., New Response Evaluation Criteria in Solid Tumours: Revised Recist Guideline (Version 1.1). ***European Journal of Cancer Care*** 2009, **45**(2): 228-47.
18. Kluger, H.M., H.A. Tawbi, M.L. Ascierto, et al., Defining Tumor Resistance to Pd-1 Pathway Blockade: Recommendations from the First Meeting of the Sitc Immunotherapy Resistance Taskforce. ***Journal for ImmunoTherapy of Cancer*** 2020, **8**(1): e000398.
19. Ma, J., M. Liu, Y. Wang, et al., Quantitative Proteomics Analysis of Young and Elderly Skin with Dia Mass Spectrometry Reveals New Skin Aging-Related Proteins. ***Aging (Albany NY)*** 2020, **12**(13): 13529-13554.
20. Wang, H., L. Qian, Z. Shang, et al., Immobilized Titanium (Iv) Ion Affinity Chromatography Contributes to Efficient Proteomics Analysis of Cellular Nucleic Acid-Binding Proteins. ***Journal of proteome research*** 2022, **21**(1): 220-231.
21. Zhou, H., M. Ye, J. Dong, et al., Robust Phosphoproteome Enrichment Using Monodisperse Microsphere–Based Immobilized Titanium (Iv) Ion Affinity Chromatography. ***Nature Protocols*** 2013, **8**(3): 461-480.
22. Wang, H., J. Zhu, S. Li, et al., Massive Deciphering of the Tissue Nucleic Acid-Binding Proteome Via Affinity Chromatography Integrated with Data-Independent Acquisition-Based Proteomics. ***Nucleic acids research*** 2025, **53**(21).
23. Turman, M.A. and A. Mathews, A Simple Luciferase Assay to Measure Atp Levels in Small Numbers of Cells Using a Fluorescent Plate Reader. ***In Vitro Cellular & Developmental Biology. Animal*** 1996, **32**(1): 1-4.
24. Jackson, C.B., S. Gallati, and A. Schaller, Qpcr-Based Mitochondrial DNA Quantification: Influence of Template DNA Fragmentation on Accuracy. ***Biochemical and Biophysical Research Communications*** 2012, **423**(3): 441-447.
25. Hensen, F., A. Potter, S.L. van Esveld, et al., Mitochondrial Rna Granules Are Critically Dependent on Mtdna Replication Factors Twinkle and Mtssb. ***Nucleic Acids Res*** 2019, **47**(7): 3680-3698.
26. Hänzelmann, S., R. Castelo, and J. Guinney, Gsva: Gene Set Variation Analysis for Microarray and Rna-Seq Data. ***BMC Bioinformatics*** 2013, **14**: 7.
27. Liberzon, A., C. Birger, H. Thorvaldsdóttir, et al., The Molecular Signatures Database (Msigdb) Hallmark Gene Set Collection. ***Cell systems*** 2015, **1**(6): 417-425.
28. Kanehisa, M. and S. Goto, Kegg: Kyoto Encyclopedia of Genes and Genomes.

Nucleic acids research 2000, **28**(1): 27-30.

29. Kumagai, S., S. Koyama, K. Itahashi, et al., Lactic Acid Promotes Pd-1 Expression in Regulatory T cells in Highly Glycolytic Tumor Microenvironments. ***Cancer Cell*** 2022, **40**(2): 201-218.e9.
30. Lee, S.H., S. Kim, J. Lee, et al., Comprehensive Metabolomic Analysis Identifies Key Biomarkers and Modulators of Immunotherapy Response in Nsclc Patients. ***Drug Resist Updat*** 2024, **77**: 101159.
31. Shen, H., O.A. Ojo, H. Ding, et al., Hif1α-Regulated Glycolysis Promotes Activation-Induced Cell Death and Ifn-Γ Induction in Hypoxic T Cells. ***Nature Communications*** 2024, **15**(1): 9394.
32. Contreras-Baeza, Y., P.Y. Sandoval, R. Alarcón, et al., Monocarboxylate Transporter 4 (Mct4) Is a High Affinity Transporter Capable of Exporting Lactate in High-Lactate Microenvironments. ***Journal of Biological Chemistry*** 2019, **294**(52): 20135-20147.
33. Payen, V.L., E. Mina, V.F. Van Hée, et al., Monocarboxylate Transporters in Cancer. ***Molecular metabolism*** 2020, **33**: 48-66.
34. Al-Mathkour, M., Z. Chen, J. Poveda, et al., Cdk1 Drives Sox9-Mediated Chemotherapeutic Resistance in Gastric Cancer. ***Journal of Experimental & Clinical Cancer Research*** 2025, **44**(1).
35. Santamaría, D., C. Barrière, A. Cerqueira, et al., Cdk1 Is Sufficient to Drive the Mammalian Cell Cycle. ***Nature*** 2007, **448**(7155): 811-5.
36. Monzel, A.S., J.A. Enríquez, and M. Picard, Multifaceted Mitochondria: Moving Mitochondrial Science Beyond Function and Dysfunction. ***Nature Metabolism*** 2023, **5**(4): 546-562.
37. Liu, L., Y. Li, G. Chen, et al., Crosstalk between Mitochondrial Biogenesis and Mitophagy to Maintain Mitochondrial Homeostasis. ***Journal of Biomedical Science*** 2023, **30**(1): 86.
38. Clay Montier, L.L., J.J. Deng, and Y. Bai, Number Matters: Control of Mammalian Mitochondrial DNA Copy Number. ***Journal of Genetics and Genomics*** 2009, **36**(3): 125-131.
39. Mei, H., S. Sun, Y. Bai, et al., Reduced Mtdna Copy Number Increases the Sensitivity of Tumor Cells to Chemotherapeutic Drugs. ***Cell Death & Disease*** 2015, **6**.
40. Sharma, P., S. Goswami, D. Raychaudhuri, et al., Immune Checkpoint Therapy-Current Perspectives and Future Directions. ***Cell*** 2023, **186**(8): 1652-1669.
41. Galan-Cobo, A., P. Sitthideatphaiboon, X. Qu, et al., Lkb1 and Keap1/Nrf2 Pathways Cooperatively Promote Metabolic Reprogramming with Enhanced Glutamine Dependence in Kras-Mutant Lung Adenocarcinoma. ***Cancer research*** 2019, **79**(13): 3251-3267.
42. Watson, M.J., P.D.A. Vignali, S.J. Mullett, et al., Metabolic Support of Tumour-Infiltrating Regulatory T Cells by Lactic Acid. ***Nature*** 2021, **591**(7851): 645-651.
43. Goldberg, F.W., J.G. Kettle, G.M. Lamont, et al., Discovery of Clinical Candidate

Azd0095, a Selective Inhibitor of Monocarboxylate Transporter 4 (Mct4) for Oncology. ***Journal of Medicinal Chemistry*** 2023, **66**(1): 384-397.